Tuning SnO$_2$–TiO$_2$ tandem systems for dyes mineralization

Alexandru Enesca*, Luminita Isac, Luminita Andronic, Dana Perniu, Anca Duta

Center for Renewable Energy System and Recycling, R&D Institute of the Transilvania University of Brasov, Eroilor 29 Street, 500036 Brasov, Romania

ABSTRACT

Six SnO$_2$–TiO$_2$ tandem semiconductor samples were prepared by spray pyrolysis deposition using different precursor compositions and deposition temperatures. By tailoring the indium doped tin oxide layer (morphology, crystallinity) the tandem properties can be modified according to the targeted application, insuring enhanced charge separation, higher photosensitivity and reduced recombination. On the SnO$_2$ layer, the TiO$_2$ growth was proved to be almost twice faster when starting from halide precursor, compared to organo-metallic ones, at a fixed deposition temperature (400 °C). The samples were characterized by X-ray diffraction, atomic force microscopy, scanning electron microscopy, contact angle, reflectance, current density–voltage (J–V) and photocurrent measurements. The photocatalytic efficiency of the tandem systems was tested on methylene blue reference solutions and was evaluated based on the variations in the organic carbon and total nitrogen content. The result were compared with bleaching measurements, showing that mineralization could be reached up to 90% and carbon removal is more efficient compared with nitrogen compounds.

© 2013 Elsevier B.V. All rights reserved.

1. Introduction

Research and use of photosensitive materials have considerably increased in recent years and replacing mono-component structures [1,2] with tandem systems [3–5] is now recognized as an alternative for improving the light conversion efficiency. The mono-component structures consist mostly of metal oxide materials with high photosensitive properties [6,7]. The main problems exhibited by the mono-component structures are related to the high charge carriers' recombination [8] and reduced photocurrent stability [9]. A tandem system, with voltage added from two photosensitive semiconductors can represent o solution to generate a higher carrier charge concentration [10–12], by using a broader part of the solar/light energy exhibiting thus a better photo-efficiency. Additionally, the use of two semiconductors with different values of the energy levels is one of the most effective ways to reduce the recombination of electron–hole pairs [13,14]. Many coupled semiconductor systems, such as ZnO–Fe$_2$O$_3$ [15,16], ZnO–WO$_3$ [17], ZnO–SnO$_2$ [18–20], TiO$_2$–WO$_3$ [21], TiO$_2$–SnO$_2$ [22,23], TiO$_2$–CdS [24–26] have shown high photosensitive properties by increasing the charge separation and extending the energy range of photon-absorption. Further on, the tandem device concepts are based on thin film materials and technologies, which can reduce the cost of the system.

It was previously shown that obtaining bi- [27,28] or tri-component [29,30] systems should be based on energy states diagrams which can describe the suitable position of the energy levels. Issues concerning tandem photosensitive semiconductors are still to be solved, among them the most important being the bottom semiconductor – top semiconductor interface and its influence on the top layer properties.

A problem related with the optoelectronic applications is that many wide band gap semiconductor oxides are reported to be deposited on commercial conductive glass substrates which limit the flexibility in choosing the morphology because the properties of the further deposited oxides strongly depend on the bottom layer.

Therefore, the main purpose of this study is to presents an alternative, by developing conductive tin oxide-based substrates with controlled properties that can be tuned according to the prerequisites for the next deposited layer. The paper presents kinetics studies related to the nucleation and growth processes in relation with the precursor composition and the number of deposition sequences. The interface control in the tandem systems allows adding new functionalities to the existing semiconductors by altering the structure, composition, and particle/grain size with direct consequences on the investigated application as photosensitive semiconductor materials. Further on, the aim is to demonstrate the photocatalytic properties of the tandem systems, and outlines the influence of the crystalline structure, morphology and surface energy on the energy levels, electrical- and photo-conductivity.

* Corresponding author. Tel.: +40 726680794.
  E-mail address: aenesca@unitbv.ro (A. Enesca).

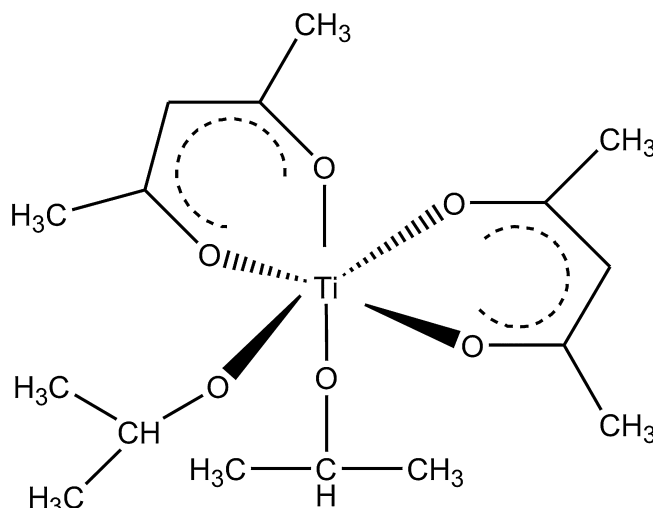**Fig. 1.** Ti((CH$_3$)$_2$CHO)$_2$(AcAc)$_2$] complex.

2. Experimental procedure

2.1. Precursor preparation

2.1.1. SnO$_2$ thin films deposition

The SnO$_2$ thin films doped with 0.1 wt% In^{3+} ions were deposited starting from a 0.05 M SnCl$_4$ solution prepared using tin chloride (SnCl$_4$, 99.99%, Sigma Aldrich), and the corresponding amounts of indium chloride (InCl$_3$, 99.99%, Sigma Aldrich) and ethanol (99.99%, C$_2$H$_6$O, Alfa Aesar). The two salts were added into the solvent and magnetically stirred for 30 min before deposition, allowing complete dissolution and homogenization.

2.1.2. TiO$_2$ thin films deposition

The TiO$_2$ films were obtained from:

- inorganic precursor (titanium chloride, TiCl$_4$, 99.99%, Sigma Aldrich); the 0.05 M TiCl$_4$ solution was obtained by mixing the salt and the solvent (ethanol, 99.99%, C$_2$H$_6$O, Alfa Aesar) under magnetic stirring for 15 min and was immediately used.
- organo-metallic precursor (titanium tetra-isopropoxide, TTIP, TiC$_{12}$H$_{28}$O$_4$, Sigma Aldrich). The 0.05 M TTIP solution was prepared by mixing the Ti-precursor with ethanol and acetylacetone (C$_5$H$_8$O$_2$), under stirring, for 15 min and was afterwards used. The ethanol: acetylacetone volume ratio was 1:0.01.

Acetylacetone is a bidentate ligand that develops keto–enol tautomeric forms; the enolic form can coordinate the metallic cations forming stabile complexes, while preventing the hydrolysis. Thus, acetylacetonate in the precursor system develops complexes with Ti^{4+} (Eq. (1) and Fig. 1), reduces the chemical reactivity of TTIP and avoids the TTIP partial hydrolysis and polycondensation, resulting in a clear, colorless and stable liquid solution.

$$Ti^{4+} + 4(CH_3)_2CHO^- + 2AcAcH \rightarrow [Ti((CH_3)_2CHO)_2(AcAc)_2]$$

$$+2(CH_3)_2CHOH \qquad (1)$$
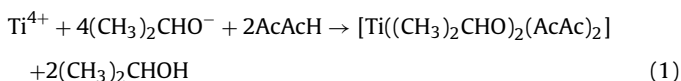
2.2. Deposition technique

Tin oxide (SnO$_2$) and titanium oxide (TiO$_2$) were obtained by spray pyrolysis deposition (SPD) using a 6 axes robot (ABB, model IRB5400) with a control software (ABB, IRC5P control system) and a heating ceramic plate (Ceram, model HP1212M).

Table 1
Values of the deposition temperature.

Sample name	T_{SnO_2} (°C)	T_{TiO_2} (°C)
Sn_300_TiCl$_4$	300	300
Sn_350_TiCl$_4$	350	350
Sn_400_TiCl$_4$	400	400
Sn_300_TTIP	300	300
Sn_350_TTIP	350	350
Sn_400_TTIP	400	400

The substrate was 2×2 cm^2 microscopic glass, cleaned by successive immersion in ethanol and acetone, using an ultrasonic bath. The carrier gas was air at 1.4×10^5 Pa and the distance between the spraying nozzle and the substrate was fixed at 15 cm. The optimized number of spraying sequences for SnO$_2$ was 25, with 30 s breaks between two pulses and with pulse duration of about 10 s. The TiO$_2$ films were deposed using an optimized number of 17 deposition sequences, with 30 s breaks between two pulses and with pulse duration of about 10 s. The deposition temperatures are presented in Table 1.

2.3. Characterization methods

The crystalline structures were investigated by X-ray diffraction (XRD, Bruker D8 Discover Advanced Diffractometer) using a locked-couple technique with 0.002° scan step and 0.01 s/step. The morphology of the nanocomposite structures was studied using Atomic Force Microscopy (AFM, NT-MDT model BL222RNTE) and scanning electron microscopy (SEM, Hitachi model S-3400 N type II). The AFM images were taken in semicontact mode with Si-tips (NSG10, force constant 0.15 N/m, tip radius 10 nm) and the results were processed with the dedicated software (NT-MDT, NovaSoft). The SEM pictures were obtained in secondary electron regime at high vacuum (10^{-3} Pa, 3 nm at 30 kV). Static contact angle measurements were used to evaluate the surface energy, based on the sessile drop method (OCA-20 Contact Angle-meter, DataPhysics Instruments). The contact liquids were glycerol and ethylene glycol. Energy dispersive X-ray measurements (EDS, Thermo) were done for elemental analysis, based on the energy values corresponding to each element in the samples.

The layer thickness was evaluated by spectroscopic measurements after each deposition sequence [31,32]. The reflectance spectra were recorded at fixed angle (6°) using an UV-VIS-NIR spectrometer (Perkin Elmer Lambda 950). The growth kinetics of the films was estimated based on thickness measurements correlated with the number of deposition sequences and the precursor composition.

The electrical (current density–voltage curves) and opto-electric (photocurrent) properties were investigated using a multichannel potentiostat (PAR Instruments, model HM 8143) with a frequency analyzer, a monochromator (Acton, SpectraPro 2150i) and a UV–VIS light source (Oriel, model 7123). The current–voltage analyses were made using two graphite contacts: one for the applied voltage, and the second, on top of the layers, used as current receptor. Both contacts were placed at constant distance (1.5 cm) on each sample. The photocurrent was measured by irradiating the sample from the back side. The band gap values were evaluated based on spectroscopic measurements (UV-VIS transmittance, Perkin Elmer Lambda 25 UV/VIS) [30,33] and the position of the energy levels were calculated using a method previously described [30,34].

2.4. Photocatalysis experiments

The photodegradation reactor consists of a static cylindrical flask, open to air. Three F18W/T8 black light tubes (Philips) (UVA light, typically 340–400 nm, $\lambda_{max} = 365$ nm), placed annular to the
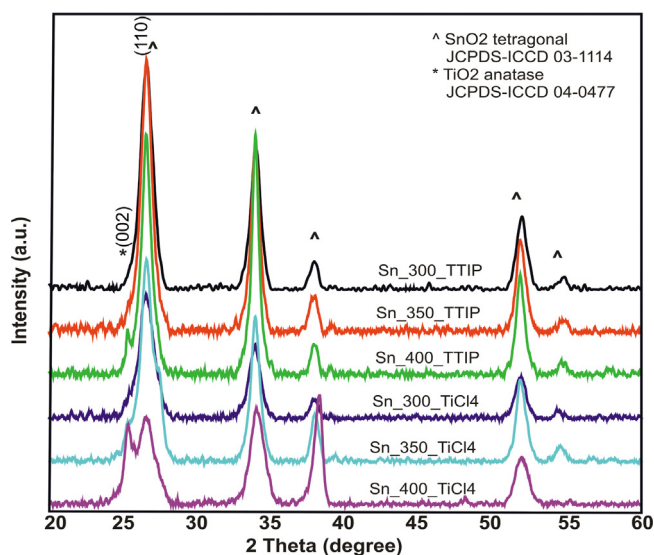
Fig. 2. XRD patterns of the samples.

photoreactor were used for photocatalysis. The system worked in a static regime and was totally closed during the experiments [35].

The pollutant dye system tested in this work was 0.0125 mM methylene blue (99.8%, Merck) prepared by dissolving the powder in ultra pure water (Direct-Q3 Water Purification system). The photocatalytic degradation/mineralization of methylene blue was evaluated using a total organic and total nitrogen analyzer (TOC-L + TNM-L, Shimadzu TOC-LCPH). The measurements were made using the auto-sampling mode, at 1 h interval during 6 h.

Each sample ($2 \times 2\,cm^2$) was inserted into a 25 mL quartz beaker and left 1 h in dark, to reach equilibrium. The equilibrium concentration in dark was set as reference in the further photocatalysis experiments.

The bleaching efficiency was evaluated based on the UV–VIS calibration curve, at 665 nm (Perkin Elmer Lambda 950), considering the initial, c_0, and current concentration, c, hourly measured up to 6 h of photocatalysis:

$$\eta = \frac{c_0 - c}{c} \cdot 100 \qquad (2)$$

3. Results and discussions

The diffraction data (Fig. 2) indicate that all samples contain tetragonal SnO_2, and there is no diffraction peak corresponding to indium oxide or to any ternary compounds formed as a consequence of the doping process (indium dopant was used to improve the electrical conductivity of the bottom layer [36,37]). Crystalline SnO_2 is important as tandem component for the targeted optoelectrical properties but also as deposition substrate for TiO_2. The diffraction analysis shows that at 300 °C, regardless the titanium

precursor, there is no signal corresponding to crystalline TiO_2. When the temperature increases with 50 °C, the small diffraction line of anatase TiO_2 overlaps the signal of tetragonal SnO_2. Finally, if the deposition temperature was fixed at 400 °C, anatase TiO_2 could be clearly differentiated from the tetragonal SnO_2.

Considering the (1 1 0) plane for SnO_2 and (0 0 2) plane for anatase TiO_2, the crystallite sizes (D), were calculated (Table 2) using the Scherrer formula [38,39].

The crystallite sizes were further correlated with the roughness values obtained from the AFM analyses (Fig. 3). For the indium doped SnO_2 layers, the crystallite sizes and the roughness were measured before the TiO_2 deposition and the data show that larger crystallites form smooth thin films, with low roughness (15.8 nm). When the crystallite size decreases, less uniform layers are obtained, with less ordered arrangements and increased heterogeneity in the aggregates sizes and geometry having higher roughness (about 35 nm).

The influence of the TiO_2 deposition temperature on the morphology of the final tandem was observed by AFM measurements and roughness variation. At 300 °C the sample exhibited roughness values between 2 and 4.5 nm regardless the precursor composition. These values indicate that titanium dioxide with regular structure (Fig. 3a and d) covers the substrate non-uniformities. The absence of the TiO_2 diffraction line in the XRD measurement can be explained by a predominant amorphous TiO_2 phase, as result of the low deposition temperature [40].

When increasing the deposition temperature, to 350 °C or 400 °C the influence of the precursors becomes significant. Both for titanium chloride and TTIP, the roughness increases by increasing temperature, but the maximum values are quite different: 33 nm in inorganic precursor systems and 21 nm in the organometallic system. The differences might be caused by the different vapor pressures/volatility of the precursors systems, with significant effect on the nucleation and crystal growth kinetics [41]. At 20 °C titanium chloride vapor pressure is P = 1.1 kPa ($TiCl_4$, boiling point = 136.7 °C) which is higher compared with titanium tetra-isopropoxide vapor pressure P = 0.01 kPa (TTIP, boiling point = 232 °C [42,43]); consequently nucleation and growth are faster when using halides precursors because of the larger amount of reactive precursors [44]. Acetylacetonate as such has no significant influence on the thermodynamic parameters considering that the vapor pressure (0.3 kPa at 20 °C) is much lower as compared to halide precursors. Because there is no clear indicator of preferential growth, crystallites size and packing would have the most significant influence on the surface roughness. The ratio between the aggregate sizes (evaluated by Fourier transformation of AFM/3D topography measured in semi-contact mode) and the crystallite size (calculated from Scherrer formula based on the XRD data) gives the average number of crystallites in the aggregates. The samples which exhibited high roughness were formed by aggregates containing an average number of 4 crystallites (Table 2). At higher deposition temperatures, tin oxide also gets more compact (an average of 2 crystallites per aggregate at 300 °C and an

Table 2
Crystallite size and roughness values.

Sample	Crystallite size (Å)		Roughness (nm)		Average no. of crystallites in the aggregates	
	SnO_2	TiO_2 anatase	SnO_2	TiO_2 anatase	SnO_2	TiO_2 anatase
Sn_300_TiCl$_4$	87.4	–	15.8	4.4	2	–
Sn_350_TiCl$_4$	81.8	81.8	35.4	19.7	4	2.5
Sn_400_TiCl$_4$	81.4	82.4	35.6	32.9	4	4
Sn_300_TTIP	87.4	–	15.8	2.3	2	–
Sn_350_TTIP	81.8	81.5	35.4	10.3	4	1.25
Sn_400_TTIP	81.4	82	35.6	20.7	4	2.5
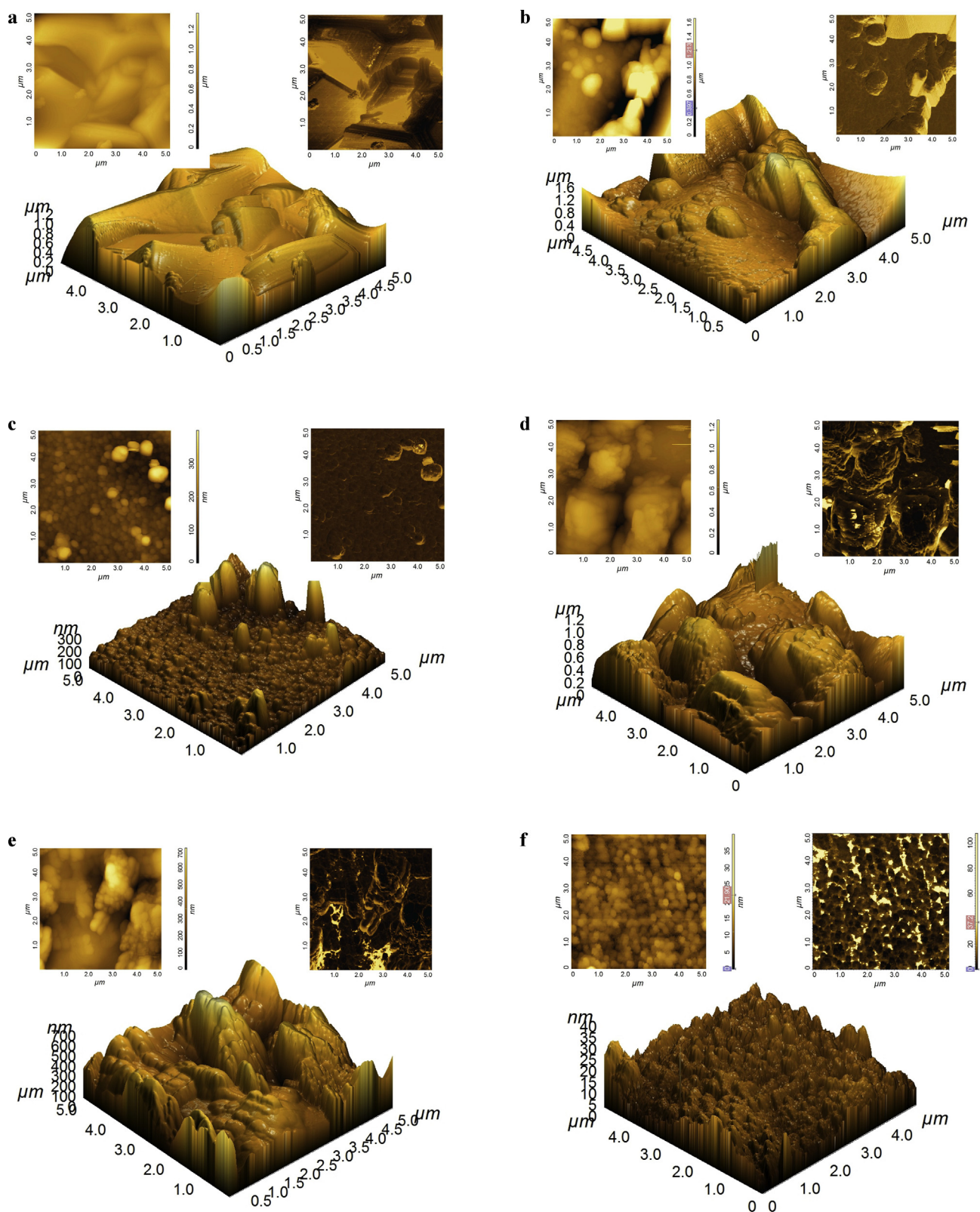
Fig. 3. The 3D (center image), 2D (left corner) and phase (right corner) AFM analysis of (a) Sn_300_TiCl₄, (b) Sn_350_TiCl₄, (c) Sn_400_TiCl₄, (d) Sn_300_TTIP, (e) Sn_350_TTIP and (f) Sn_400_TTIP samples.

average of 4 at higher temperatures); the effect of the precursor type was evident for the TiO_2 deposition, when the inorganic precursor supported the formation of aggregates consisting, on average, of a double number of crystallites, as compared to TTIP.

While approaching the substrate, the precursor droplets in the aerosol are heated and the solvent vaporizes, resulting in a gradually increased concentration of the Ti-precursor in the droplet. Highly concentrated droplets reaching the substrate have a fast
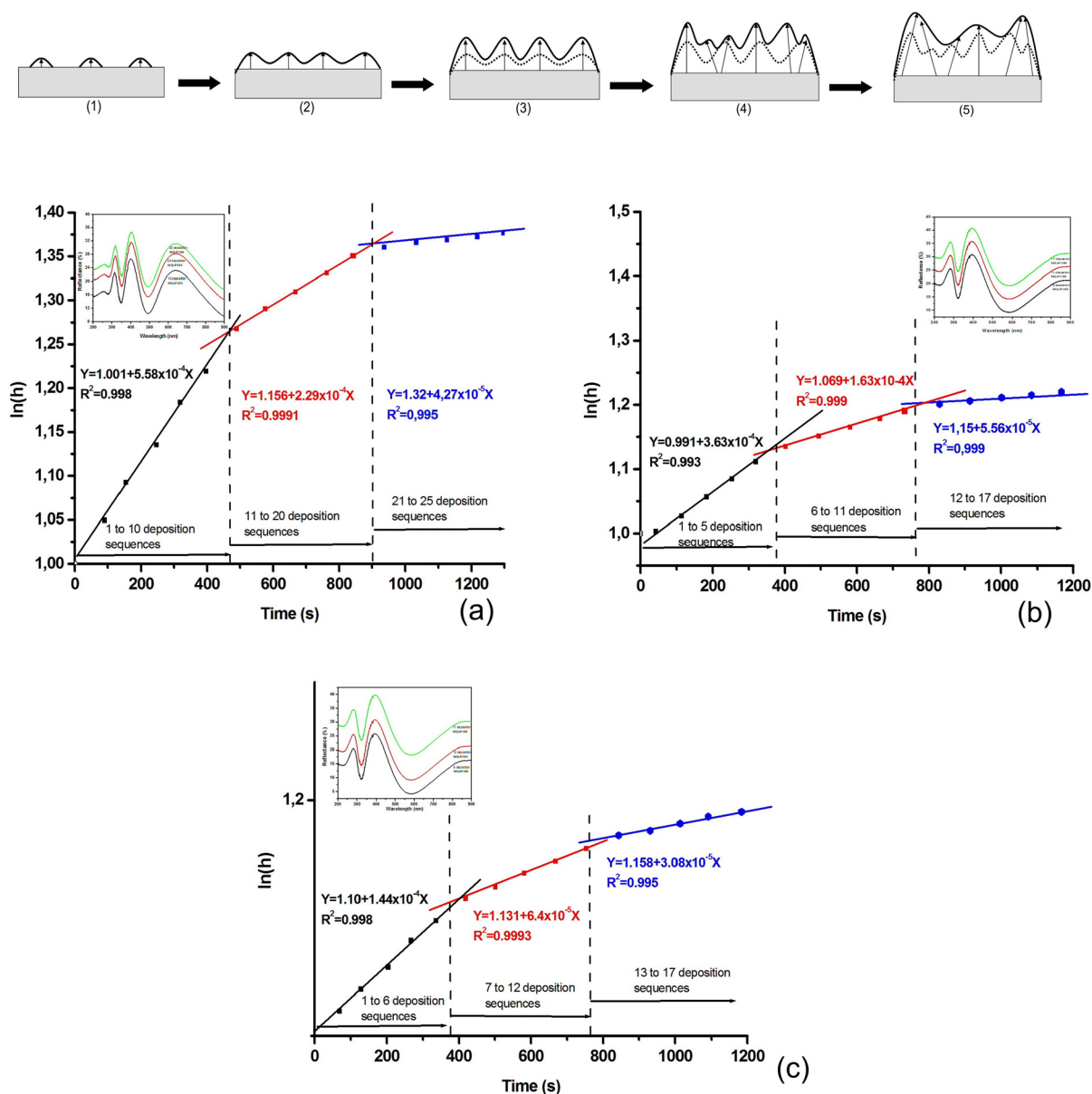
Fig. 4. Layers' formation kinetics and the regression coefficients for (a) SnO_2 obtained from $SnCl_4$, (b) TiO_2 obtained from $TiCl_4$ and (c) TiO_2 obtained from TTIP.

nucleation rate, as it was the case of the inorganic precursor. Further growth is also fast and the result is a rough structure. The organic precursor needs a longer time to complete pyrolysis, consequently the nucleation sites have a more random distribution on the active sites filling the fractured morphology and leading to less rough films.

These results show a possible control of the tandem systems interface. Therefore, the kinetics of the layers' formation was further investigated by measuring the layers thickness, for the samples with the highest crystallinity obtained at 400 °C, Fig. 4. The deposition parameters (i.e. precursor concentration, pressure, the break between the deposition sequences) for each layer were previously optimized and are presented elsewhere [45,46]. One deposition sequence took 10 s, and the break between two deposition sequences was 30 s for SnO_2 and 40 s for TiO_2. The total number of deposition sequences was 25 for SnO_2 and 17 for TiO_2 from $TiCl_4$ or from TTIP. The final thickness of the samples was 320 nm for SnO_2, 197 nm for TiO_2 from $TiCl_4$ and 180 nm for TiO_2 from TTIP.

As Fig. 4 shows, five steps can be theoretically described; still the kinetic data show that actually the process runs in three stages, all of them following the first order kinetics with different rate constants (Table 3). The first stage is nucleation (1) and the formations of the incipient layer (2) for which the highest growth rate corresponds to the samples obtained from halide precursors [47]. The optimum number of deposition sequences, obtained form the kinetic evaluation was 10 for SnO_2, 5 for TiO_2 from $TiCl_4$ and 6 for TiO_2 from TTIP. The second stage corresponds to the formation of the bulk structure based on aggregates sintering (3 & 4). This growth rate can

Table 3
Rate constants for the films formation mechanisms [s^{-1}].

Thin film	Nucleation (steps 1 & 2)	Growth and sintering (steps 3 & 4)	Densification (5)
SnO_2	5.58×10^{-4}	2.29×10^{-4}	4.27×10^{-5}
TiO_2 from $TiCl_4$	3.63×10^{-4}	1.63×10^{-4}	5.56×10^{-5}
TiO_2 from TTIP	1.44×10^{-4}	6.41×10^{-5}	3.08×10^{-5}

a

b

c

d

e

f
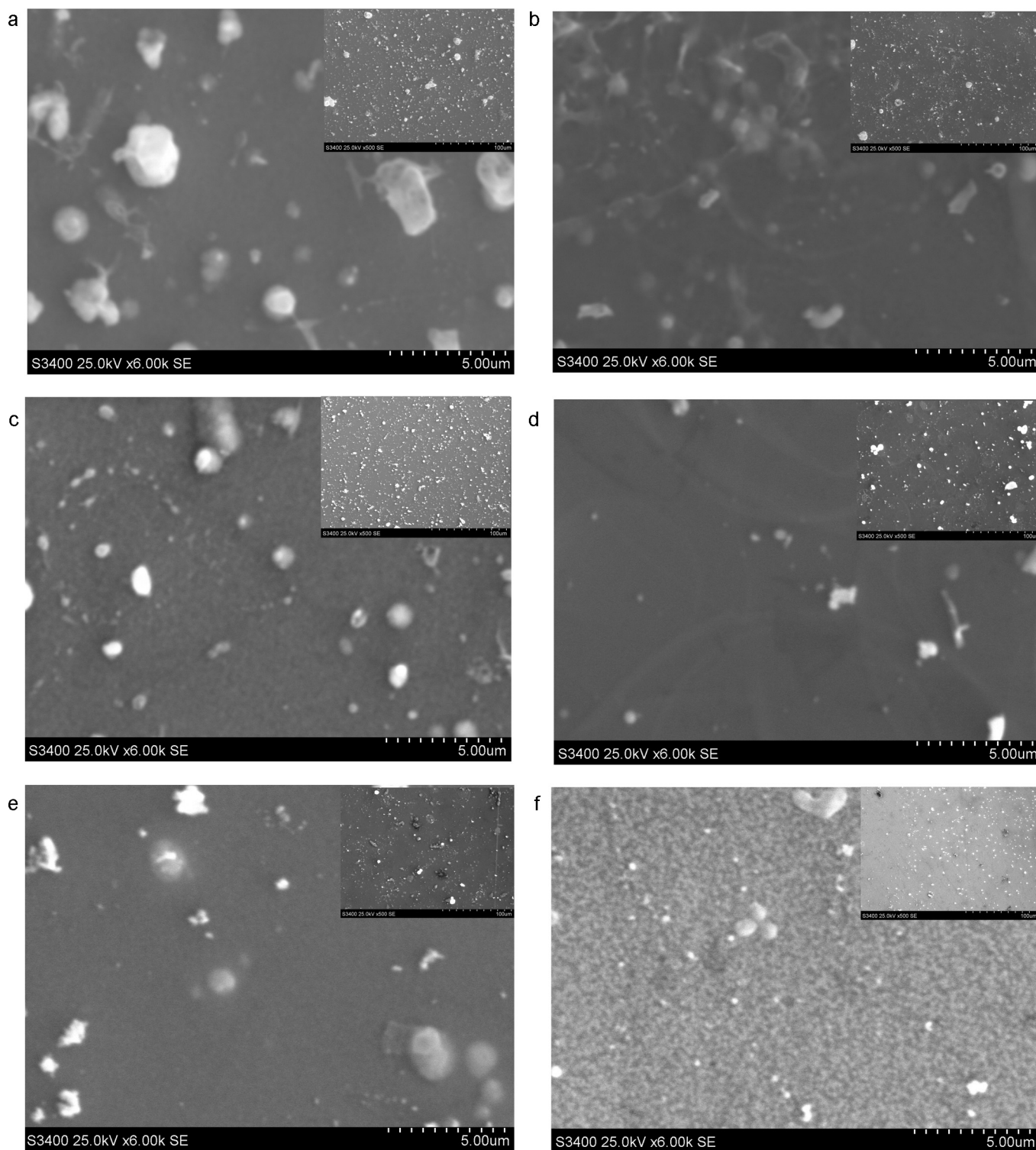
Fig. 5. The SEM images of (a) Sn_300_TiCl$_4$, (b) Sn_350_TiCl$_4$, (c) Sn_400_TiCl$_4$, (d) Sn_300_TTIP, (e) Sn_350_TTIP and (f) Sn_400_TTIP samples.

well be corroborated with the roughness values as the highest rate corresponds to the much rougher SnO$_2$. The last stage corresponds to the film densification and for all samples the change in thickness is relatively low [48]. Densification can be the result of the release of residual by-products or of an in situ annealing process.

The SEM analysis (Fig. 5) was made in high vacuum without metallic coverage and has shown that all samples contain film and residual powder. Film formation ideally requires the

pyrolysis process on the substrate but the initial steps can begin above this where the temperature is high enough to induce complete solvent evaporation and reaction in the smallest droplets, with powder formation [49]. The samples obtained from TTIP had lower powder coverage because of their lower volatility. The samples surface is free of cracks and has a porous morphology (Sn_400_TiCl$_4$ – Fig. 5c, Sn_350_TTIP – Fig. 5d and Sn_400_TTIP – Fig. 5e).
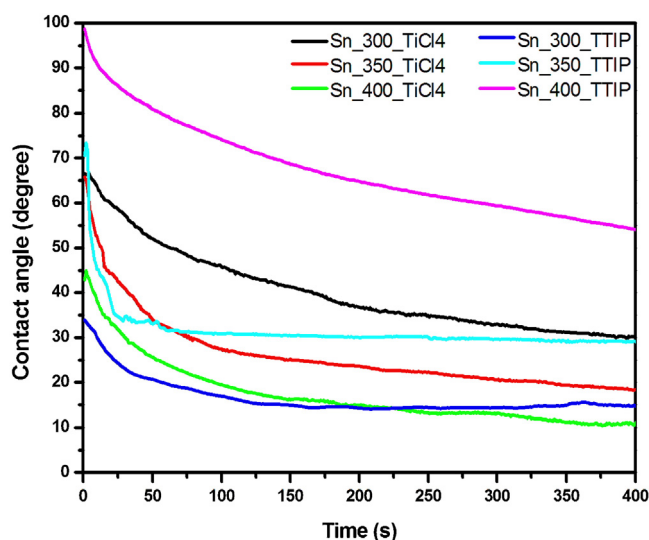
Fig. 6. Contact angle measurements with glycerol.

Titanium oxide and tin oxide were used as photocatalyst for pollutants removal from different aqueous media and, in this surface application, wettability and surface tension are important parameters [50]. Contact angle measurements (Fig. 6) were done using two liquids with different polarities: glycerol (with the polar component of the surface energy $\sigma^p = 41.50$ mN/m and the dispersive component of $\sigma^d = 21.20$ mN/m) and ethylene glycol (with the polar component $\sigma^p = 19$ mN/m and the dispersive component $\sigma^d = 29$ mN/m). The contact angle profile for ethylene glycol was not presented because of the fast absorption rate (5 s). Using the Fowkes equation (Eq. (3)), based on the dispersive and the polar components of the liquid–solid interface, the surface energy values were calculated for each sample and are presented in Table 4.

According to Fowkes [51]:

$$\sigma_{LV}(1 + \cos\theta) = 2[(\sigma_{LV}^p \sigma_{SV}^p)^{1/2} + (\sigma_{LV}^d \sigma_{SV}^d)^{1/2}] \qquad (3)$$

where σ_{LV}^p, σ_{SV}^p, σ_{LV}^d, σ_{SV}^d are polar and dispersed components of the liquid- and solid-surface energies, respectively.

As expected for oxides, the samples have a predominant polar component of the surface energy (see Table 4) which indicates the hydrophilic character and wettability, making them suitable candidates for applications in aqueous solutions (as photocatalysts or photoanodes for photoelectrochemical cells) [52]. The surface polarity increases for the samples obtained at higher deposition temperatures, as result of an increased crystallinity and the formation of much rougher (fractured) morphologies as confirmed by the XRD and AFM results. It is also to be noticed that the metal precursors (TiCl₄) lead to higher energy surfaces, suitable for adsorption processes [53].

Considering that both SnO_2 and TiO_2 are photosensitive materials, the mechanisms for photoinduced hydrophilicity was initiated

Table 4
The polar and dispersive component of the surface energy.

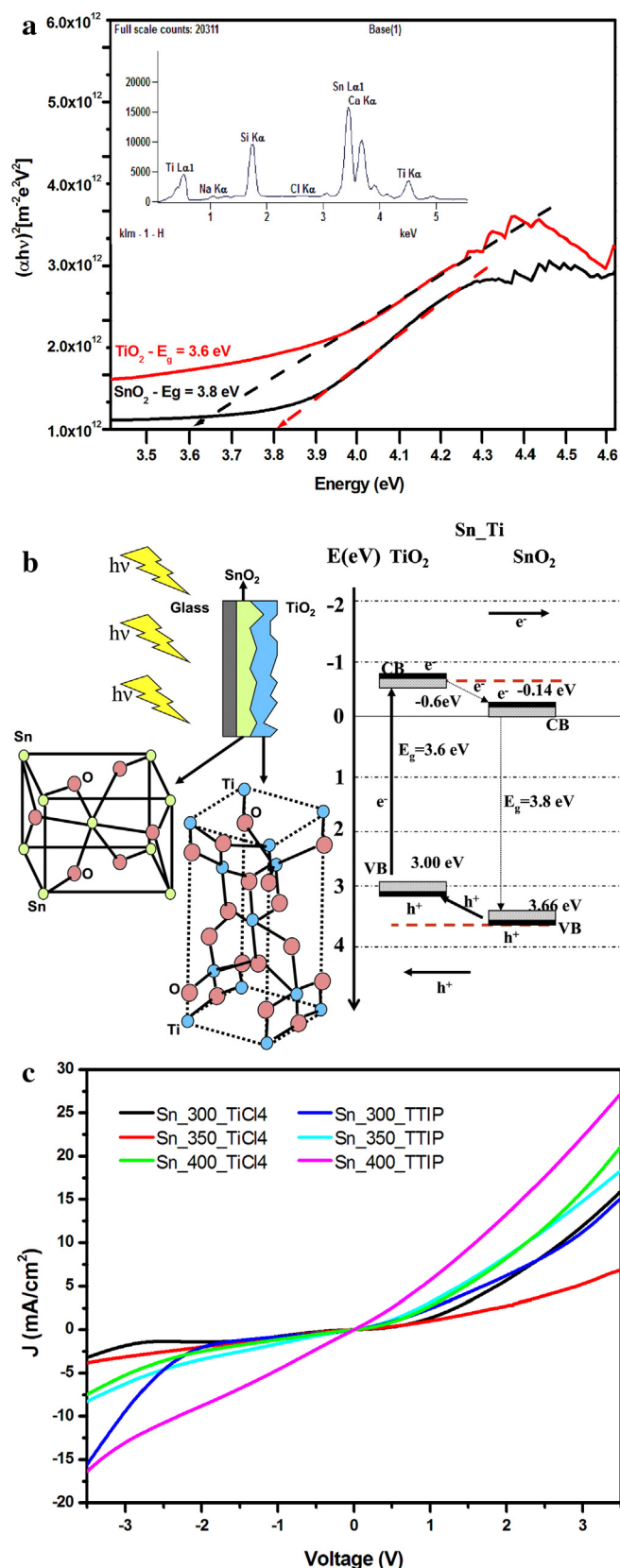| Sample	Surface energy σ (mN/m)	Polar component σ^p (mN/m)	Dispersive component σ^d (mN/m)
Sn_300_TiCl₄	43.21	27.34	15.87
Sn_350_TiCl₄	47.63	36.25	11.38
Sn_400_TiCl₄	73.44	62.17	11.27
Sn_300_TTIP	21.59	14.43	7.16
Sn_350_TTIP	29.18	22.86	6.32
Sn_400_TTIP	48.35	39.68	8.67

Fig. 7. Band gap estimation based on transmittance spectra – inset: EDS analysis (a), energy level diagram (b) and current density–voltage measurements (c).
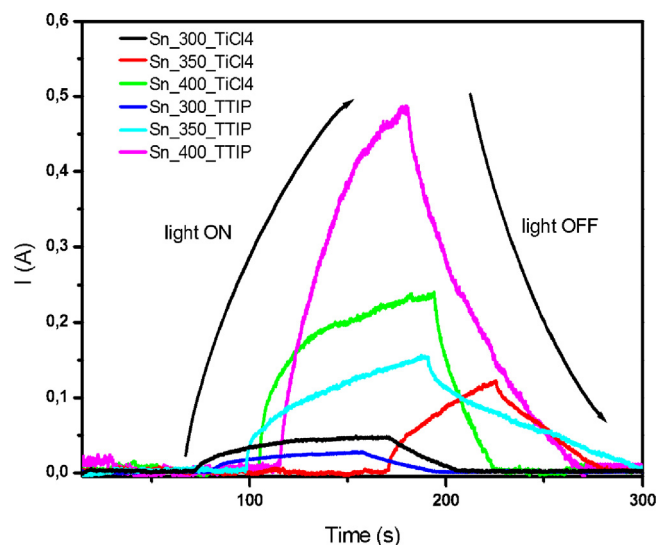
Fig. 8. Photocurrent measurements of the samples.

by holes formed during the deposition (especially during step 5) that react with the surface lattice oxygen atoms [54,55] (Eq. (4)):

$$V_O^{\bullet\bullet} + 1/2\,O_2 \rightarrow O_O^x + 2h^\bullet \qquad (4)$$

The electrical properties measurements were developed to understand and control the carrier charge mobility in the tandem system. The band gap values (Fig. 7a) were obtained based on the transmittance spectra [30,33] and using the Tauc plot, $(\alpha h\nu)^2$ vs. $h\nu$. The method of evaluating the suitable position of the energy levels (E_g, E_c, E_v) was previously presented [30,34]. The EDS spectrum (Fig. 7a, inset) shows the energy values corresponding to the layers components (titanium, tin and oxygen) but also signals from elements from the glass substrate (sodium, chloride, silicon, calcium). Compatible crystalline structures and free defects interfaces represent prerequisites for efficient carrier charge generation and mobility.

The highest electrical conductivity (Fig. 7c) corresponds, as expected [56], to the samples with the highest crystallinity (Sn_400_TiCl₄ and Sn_400_TTIP). These crystalline structures (tetragonal for SnO₂ and anatase for TiO₂) support the formation of continuous interfaces between the layers and reduce charge recombination. Considering the bands structure (Fig. 7b), electrons flow into the SnO₂ under layer, while holes oppositely diffuse into the TiO₂ upper layer. A better charge separation in the coupled film was the result of the fast electron-transfer process from the conduction band of TiO₂ to that of SnO₂. Thus, the charge recombination was significantly suppressed in the coupled film, as compared to the single films [57]. The conduction band (CB) edges of TiO₂ and SnO₂ are conveniently located at −0.6 and −0.14 eV (vs. normal hydrogen electrode, NHE), while the valence band (VB) edge of SnO₂ (+3.66 eV) is much lower than that of TiO₂ (+3.00 eV), suitable positioned for the charge carrier flow trough the tandem system. Lower electrical conductivity was identified for the samples where the crystalline anatase TiO₂ structure was not confirmed by XRD measurements. The ionic diffusion trough the bulk will not significantly influence the electrical conductivity because titanium and tin ions have the same oxidation state [58].

Additionally, photocurrent measurements (Fig. 8) allow evaluating the photosensitive properties of the layer, as this is a key property in photocatalysis where the first step is the photogeneration of charge carriers that will generate the oxidative species [59]. The photosensitivity follows the same trend as the electrical conductivity (best response for Sn_400_TiCl₄ and
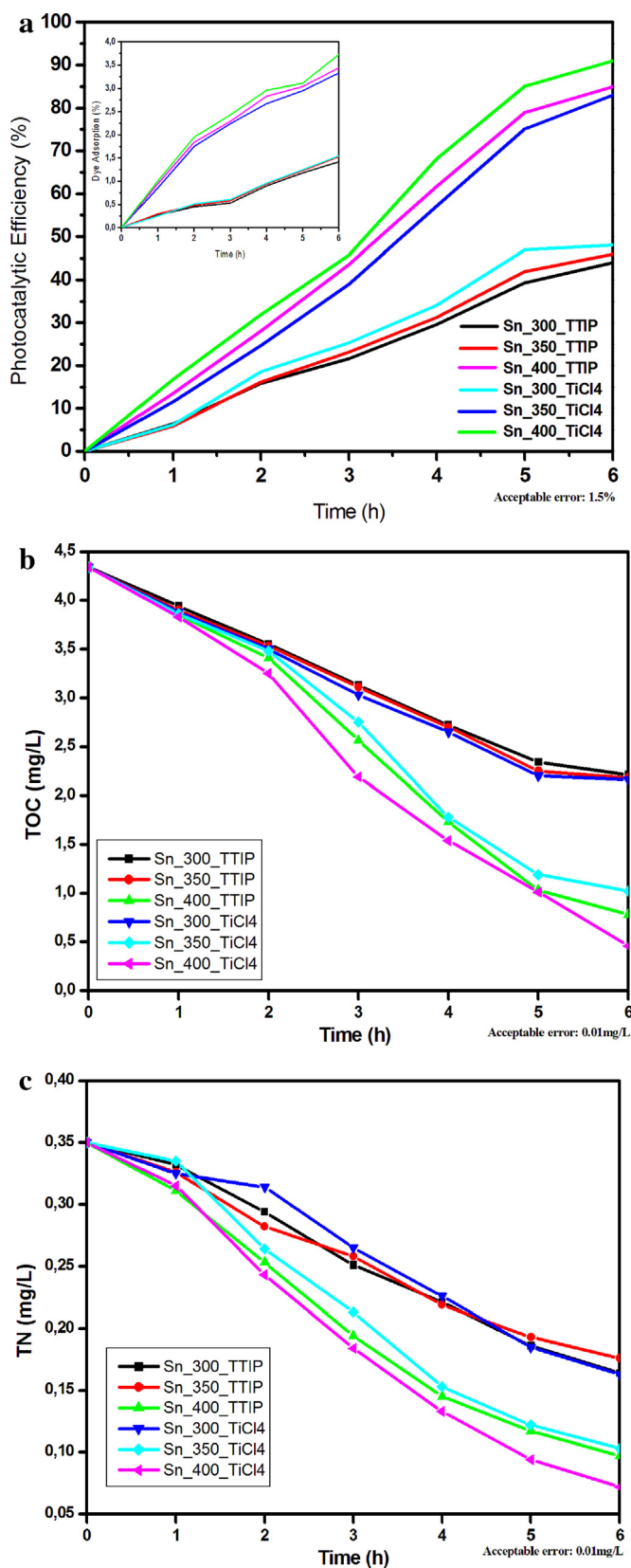

Fig. 9. Photocatalytic activity of the tandem systems: (a) bleaching evolution (inset: bleaching in dark), (b) total organic carbon (TOC) and (c) total nitrogen (TN).

Sn_400_TTIP) and confirmed the correlation between the energy level diagram and charge carrier generation (especially electrons). The lower photocurrent values were a consequence of the charge carrier recombination and of the trapping defects in bulk and at the interfaces [60]. In the tandem system, two type of trapping defects could be identified: (a) extrinsic, commonly located at the interfaces and (b) intrinsic, in the bulk. These defects were responsible for limiting the photocurrent saturation [59,60].

The photocatalytic process is designed to remove pollutants by oxidation. Partial oxidation may remove the color (bleaching) but can end up in further polluting or toxic by-products, therefore full mineralization is targeted. Consequently photocatalytic investigations were (Fig. 9) complementarily done by measuring bleaching and the organic carbon and nitrogen content evolution during 6 h. Comparative bleaching studies were done under UV irradiation (Fig. 9a) and in dark (Fig. 9a, inset) for the same time interval. The results show that bleaching in dark (which is consistent with adsorption) has a low evolution and attempt 3.7% after 6 h. Under irradiation the photocatalytic process is activated and the efficiency increases up to 91% (for Sn_400_TiCl$_4$). Under irradiation, adsorption and photocatalytic oxidation are simultaneous and, as the results show, the process was well optimized, having the adsorption rate lower than the photocatalytic oxidation, at the solid (film)–liquid interface [61,62].

The dye degradation was low in the first hour of photocatalytic activity due to the dye absorbed during the conditioning process in dark, but rapidly increased during the next 4 h when the carbon and nitrogen content was half (Sn_300_TTIP, Sn_350_TTIP, Sn_300_TiCl$_4$) and quarter (Sn_400_TTIP, Sn_350_TiCl$_4$, Sn_400_TiCl$_4$) of the initial value. The highest photocatalytic activity corresponded to the samples which exhibited better electrical conductivity and photosensitivity (Sn_400_TTIP and Sn_400_TiCl$_4$). The higher rate of charge carrier generation in the Sn_400_TTIP and Sn_400_TiCl$_4$ tandem systems (multiple charge injection) were detected in J–V and photocurrent measurements, and contributes to the formation of the oxidative species (Eqs. (5) and (6)).

$$Photocat + h\upsilon \rightarrow e^- + h^\bullet \tag{5}$$

$$h^\bullet + H_2O(Photocat) \rightarrow {}^\bullet OH(Photocat) + H^+ \tag{6}$$

The results confirm that a crystalline structure is required for better charge generation, increased mobility and low recombination and, in the photocatalytic process, the porous morphology with higher specific surface and a large number of active sites represents and advantage. Consequently, the Sn_400_TTIP, Sn_350_TiCl$_4$ and Sn_400_TiCl$_4$ samples are good candidates for photosensitive applications.

After 6 h of photocatalysis, for the best tandem film (Sn_400_TiCl$_4$) the bleaching efficiency is 91%, carbon removal was almost complete (above 90%), while less than 30% of the nitrogen from the initial methylene blue molecule was still resident in the solution, indicating that the tandem system was efficient and mainly promoted dye's mineralization.

4. Conclusions

Six different samples were prepared by SPD using different precursor composition and deposition temperatures. Well defined crystalline structures were observed for the SnO$_2$ and TiO$_2$ when the deposition temperature was 400 °C. The samples with SnO$_2$ and TiO$_2$ crystalline structure had a porous morphology and higher roughness. Depending on the precursor type, the samples follow a first order mechanisms with different nucleation, growth and densification rates, resulting in different and tunable morphologies, with wetting behavior and a predominant polar component in the surface energy.

The samples Sn_400_TiCl$_4$ and Sn_400_TTIP had optimal electrical conductivity and photosensitivity. The presence of crystalline structure (tetragonal for SnO$_2$ and anatase for TiO$_2$) facilitated the formation of continuous interfaces and induced a better charge separation in the coupled film. These properties are well fitting the photocatalysis requirements, and experiments done on methylene blue showed a carbon removal up to 90% in mineralization processes.

References

[1] S.Y. Yang, Y.S. Choo, S. Kim, S.K. Lim, J. Lee, H. Park, Appl. Catal. B: Environ. 111–112 (2012) 317–325.
[2] M. Zaied, E. Chutet, S. Peulon, N. Bellakhal, B. Desmazières, M. Dachraoui, A. Chaussé, Appl. Catal. B: Environ. 107 (2011) 42–51.
[3] K. Yamada, R. Fukuda, K. Yamamoto, Mol. Cryst. Liq. Cryst. 566 (2012) 193–201.
[4] D.H. Jun, C.Z. Kim, H. Kim, J. Semiconductor Technol. Sci. 9 (2009) 91–97.
[5] K.J. Kumar, N.R.C. Raju, A. Subrahmanyam, Surf. Coat. Technol. 205 (2011) S261–S264.
[6] N.R. Mathews, Sol. Energy 86 (2012) 1010–1016.
[7] H. Kim, H.H. Park, Ceram. Int. 38 (2012) S609–S612.
[8] S. Kment, H. Kmentova, P. Kluson, J. Krysa, Z. Hubicka, V. Cirkva, I. Gregora, O. Solcova, L. Jastrabik, J. Colloid Interface Sci. 348 (2010) 198–205.
[9] M. Li, L. Zhao, L. Guo, Int. J. Hydrogen Energy 35 (2010) 7127–7133.
[10] M. Bronzoni, M. Stefancich, S. Rampino, Thin Solid Films 520 (2012) 7054–7061.
[11] P.C. Lansåker, K. Gunnarsson, A. Roos, G.A. Niklasson, C.G. Granqvist, Thin Solid Films 519 (2011) 1930–1933.
[12] W. Vallejo, C.A. Arredondo, G. Gordillo, Appl. Surf. Sci. 257 (2010) 503–507.
[13] M. Zhang, G. Sheng, J. Fu, T. An, X. Wang, X. Hu, Mater. Lett. 59 (2005) 3641–3644.
[14] F. Fang, Q. Li, J.K. Shang, Surf. Coat. Technol. 205 (2011) 2919–2923.
[15] Y. Guo, H. Wang, C. He, L. Qiu, X. Cao, Langmuir 25 (2009) 4678–4684.
[16] S.W. Bennett, A.A. Keller, Appl. Catal. B: Environ. 102 (2011) 600–607.
[17] C. Yu, K. Yang, Q. Shu, J.C. Yu, F. Cao, X. Li, Chin. J. Catal. 32 (2011) 555–565.
[18] B.J. Babu, S. Velumani, R. Asomoza, Proc. 37th IEEE Photovoltaic Specialists Conference U.S.A. 2011, 2011, 001238-43.
[19] Z. Wang, Z. Li, H. Zhang, C. Wang, Catal. Commun. 11 (2009) 257–260.
[20] W. Cun, Z. Jincai, W. Xinming, M. Bixian, S. Guoying, P. Ping'an, F. Jiamo, Appl. Catal. B: Environ. 39 (2002) 269–279.
[21] H. Tada, A. Kokubu, M. Iwasaki, S. Ito, Langmuir 20 (2004) 4665–4670.
[22] T.P. Chou, X. Zhou, G. Cao, J. Sol–Gel Sci. Technol. 50 (2009) 301–307.
[23] Y. Guo, J. Cheng, Y. Hu, D. Li, Appl. Catal. B: Environ. 125 (2012) 21–27.
[24] H. Park, W. Choi, M.R. Hoffmann, J. Mater. Chem. 18 (2008) 2379–2385.
[25] H.L. Meng, C. Cui, H.L. Shen, D.Y. Liang, Y.Z. Xue, P.G. Li, W.H. Tang, J. Alloy. Compd. 527 (2012) 30–35.
[26] Z.D. Meng, M.M. Peng, L. Zhu, W.C. Oh, F.J. Zhang, Appl. Catal. B: Environ. 113–114 (2012) 141–149.
[27] D. Joskowska, K. Pomoni, A. Vomvas, B. Kościelska, D.L. Anastassopoulos, J. Non-Cryst. Solids 356 (2010) 2042–2048.
[28] E.M. El-Maghraby, Physica B 405 (2010) 2385–2389.
[29] A. Enesca, L. Andronic, A. Duta, Appl. Surf. Sci. 258 (2012) 4339–4346.
[30] T. Mise, T. Nakada, Thin Solid Films 518 (2010) 5604–5609.
[31] A. Enesca, A. Duta, Thin Solid Films 519 (2010) 568–572.
[32] Y. Laaziz, A. Bennoun, N. Chahboun, A. Outzourhit, E.L. Ameziane, Thin Solid Films 372 (2000) 149–155.
[33] L. Andronic, L. Isac, A. Duta, J. Photochem. Photobiol. A 221 (2011) 30–33.
[34] C. Gao, J. Li, Z. Shan, F. Huang, H. Shen, Mater. Chem. Phys. 122 (2010) 183–187.
[35] M. Dudita, C. Bogatu, A. Enesca, A. Duta, Mater. Lett. 65 (2011) 2185–2189.
[36] K.Y. Pan, L.D. Lin, L.W. Chang, H.C. Shih, Appl. Surf. Sci. 273 (2013) 12–18.
[37] Y. Seki, Y. Sawada, M.H. Wang, H. Lei, Y. Hoshi, T. Uchida, Ceram. Int. 38 (2012) S613–S616.
[38] K.V. Rao, C.S. Sunandana, Solid State Commun. 148 (2008) 32–37.
[39] Y. Caglar, S. Ilican, M. Caglar, J. Alloy Compd. 481 (2009) 885–889.
[40] E.C. Muniz, M.S. Góes, J.J. Silva, J.A. Varela, E. Joanni, R. Parra, P.R. Bueno, Ceram. Int. 37 (2011) 1017–1024.
[41] A.W. Brinkman, J. Carles, Prog. Cryst. Growth Charact. Mater. 37 (1998) 169–209.
[42] D.A. Wierda, C.M. Reddy, C.C. Amato-Wierda, Surf. Coat. Technol. 148 (2001) 256–261.
[43] K.M.S. Khalil, M.I. Zaki, A.A. El-Samahy, J. Anal. Appl. Pyrol. 42 (1997) 123–133.
[44] M.Q. Wang, J. Yan, H.P. Cui, S.G. Du, Mater. Charact. 76 (2013) 39–47.
[45] A. Enesca, A. Duta, Thin Solid Films 519 (2011) 5780–5786.
[46] A. Enesca, Environ. Eng. Manag. J. 10 (2011) 1191–1196.
[47] J.H. Greenberg, J. Cryst. Growth 197 (1999) 406–412.

[48] H.K. Sanghera, B.J. Cantwell, N.M. Aitken, A.W. Brinkman, J. Cryst. Growth 237–239 (2002) 1711–1715.
[49] A. Nakaruk, D. Ragazzon, C.C. Sorrell, J. Anal. Appl. Pyrol. 88 (2010) 98–101.
[50] S. Wang, Y. Song, L. Jiang, J. Photochem. Photobiol. C 8 (2007) 18–29.
[51] D. Exerowa, N.V. Churaev, T. Kolarov, N.E. Esipova, N. Panchev, Z.M. Zorin, Adv. Colloid Interface 104 (2003) 1–24.
[52] H.U. Lee, S.C. Lee, J.H. Seo, W.G. Hong, H. Kim, H.J. Yun, H.J. Kim, J. Lee, Chem. Eng. J. 223 (2013) 209–215.
[53] X.W. Zeng, Y.X. Gan, E. Clark, L.S. Su, J. Alloy. Compd. 24 (2011) L221–L227.
[54] H.B. Jiang, L. Gao, Q.H. Zhang, J. Inorg. Mater. 18 (2003) 695–699.
[55] V.P. Santos, M.F.R. Pereira, J.J.M. Órfão, J.L. Figueiredo, Appl. Catal. B: Environ. 99 (2010) 353–363.
[56] Y.H. Lee, S.H. Im, J.A. Chang, J.H. Lee, S.I. Seok, Org. Electron. 13 (2012) 975–979.
[57] T.W. Zeng, C.C. Ho, Y.C. Tu, G.Y. Tu, L.Y. Wang, W.F. Su, Langmuir 27 (2011) 15255–15260.
[58] A. Arranz, R. Diaz, Solid State Ionics 233 (2013) 47–54.
[59] C. Liu, J. Zhang, L. Wang, Y. Shu, J. Fan, Solid State Ionics 232 (2013) 123–128.
[60] D.S. Byeon, S.M. Jeong, K.J. Hwang, M.Y. Yoon, H.J. Hwang, S. Kim, H.L. Lee, J. Power Sources 222 (2013) 282–287.
[61] L.J. Hsu, L.T. Lee, C.C. Lin, Chem. Eng. J. 173 (2011) 698–705.
[62] F. Jiang, S. Zheng, L. An, H. Chen, Appl. Surf. Sci. 258 (2012) 7188–7194.